King's Research Portal

[Link to publication record in King's Research Portal](#)

Reducing MRI Susceptibility Artefacts in Implants Using Additively Manufactured Porous Ti-6Al-4V Structures

Luke N. Carter[a], Owen Addison[b*], Nashwan Naji[c], Peter Seres[c], Alan H. Wilman[c], Duncan E. T. Shepherd[d], Liam Grover[a], Sophie Cox[a]

a. *School of Chemical Engineering, College of Engineering and Physical Sciences, University of Birmingham, Edgbaston, UK. B15 2TT*

b. *Faculty of Dentistry, Oral and Craniofacial Sciences, King's College London, Guy's Hospital, London, UK. SE1 9RT*

c. *Department of Biomedical Engineering, Faculty of Medicine and Dentistry, University of Alberta, Edmonton, Canada*

d. *Department of Mechanical Engineering, College of Engineering and Physical Sciences, University of Birmingham, Edgbaston, UK. B15 2TT*

*Corresponding Author

Abstract

Magnetic Resonance Imaging (MRI) is critical in diagnosing post-operative complications following implant surgery and imaging anatomy adjacent to implants. Increasing field strengths and use of gradient-echo sequences have highlighted difficulties from susceptibility artefacts in scan data. Artefacts manifest around metal implants, including those made from titanium alloys, making detection of complications (e.g. bleeding, infection) difficult and hindering imaging of surrounding structures such as the brain or inner ear.

Existing research focusses on post-processing and unorthodox scan sequences to better capture data around these devices. This study proposes a complementary up-stream design approach using lightweight structures produced via additive manufacturing (AM). Strategic implant mass reduction presents a potential tool in managing artefacts.

Uniform specimens of Ti-6Al-4V structures, including lattices, were produced using the AM process, selective laser melting, with various unit cell designs and relative densities (3.1% - 96.7%). Samples, submerged in water, were imaged in a 3T MRI system using clinically relevant sequences. Artefacts were quantified by image analysis revealing a strong linear relationship (R^2=0.99) between severity and relative sample density. Likewise, distortion due to slice selection errors showed a squared relationship (R^2=0.92) with sample density. Unique artefact features were identified surrounding honeycomb samples suggesting a complex relationship exists for larger unit cells.

To demonstrate clinical utility, a honeycomb design was applied to a representative cranioplasty. Analysis revealed 10% artefact reduction compared to traditional solid material illustrating the feasibility of this approach.

This study provides a basis to strategically design implants to reduce MRI artefacts and improve post-operative diagnosis capability.

1. Introduction

Structural metal implants are an increasingly common feature of modern surgery [1] with the global market for such devices projected to grow at a cumulative average growth rate of 9.4% and exceed $17.64 billion USD by 2024 [2]. This market growth is driven in part by increases in the incidence of trauma and sports related injuries, and in the prevalence of chronic musculoskeletal disorders associated with an ageing population. Such implants fulfil a variety of functions including tissue replacement, fixation, anchorage, articulation, and cosmetic reconstruction. However, the expanded clinical use is associated with a concomitant increase in the number of cases presenting with post-operative complications or a need to investigate structures adjacent to the implanted device. In both scenarios detailed medical imaging of the structures near the metallic object is required for diagnostic and monitoring purposes.

Magnetic Resonance Imaging (MRI) is one such method and provides a powerful non-ionising approach to visualise anatomical structures, identify irregularities, highlight post-operative complications, and support molecular imaging. Since its inception, MRI systems have gradually increased in magnetic field strength enabling acquisition of higher quality data due to improved signal-to-noise ratio. 3T systems are common in clinical practice with research systems having field strengths several times greater than this, up to 11T [3]. Furthermore, the use of gradient-echo sequences, as oppose to spin-echo, has reduced data acquisition times and enhanced image contrast versatility [4]. However, these system advances have increased the severity of imaging artefacts caused by magnetic susceptibility differences between the implant material and the surrounding tissue. An article by Sinclair & Scoffings [5] remarks that, whist MRI shows a superior ability to diagnose infection compared with CT, the technique is often rendered useless by the presence of nearby metal structures.

Brain imaging is a key application for MR techniques, however metal cranioplasties may limit or prevent accurate imaging due the production of susceptibility artefacts. Specifically, MRI has been shown to support the diagnosis of empyema following cranioplasty [6], provide early diagnosis of infection without typical symptomatic indicators [7], and identify cerebral microbleeds [8] using T2*-weighted gradient-echo-imaging sequences. This is of particular importance as one study by Lee *et al.*

[9] over a ten year period reported 'infection and implant extrusion' and 'intracranial haemorrhage' to occur in 9.05% and 1.65% of cranioplasty cases respectively.

The titanium alloy, Ti-6Al-4V, is a common substrate for medical implants due to its biocompatibility, corrosion resistance, and mechanical properties which are suitable for a wide variety of applications. Metallic implants made from titanium alloys have also been shown to result in lower post-operative infection rates compared to polymeric alternatives [10], making it an attractive alternative material. Titanium is generally considered non-magnetic, generating insignificant forces in a strong magnetic field, and safe to be present in a clinical MRI system without risk of injury to the patient. It is however weakly paramagnetic with a susceptibility, χ, of approximately 1.78×10^{-4} [11] and will become magnetised within an MRI field resulting in susceptibility artefacts in the scan data. Ultimately, these artefacts can dramatically impede the use of MRI to visualise the tissue surrounding implants, and therefore hinder future investigations in the region or diagnosis of post-operative complications

A susceptibility artefact is either a loss of signal or distortion in the MRI image due to changes in the magnetic field from the presence of the implant. Artefacts arise as a result of three distinct mechanisms. Firstly, slice selection errors can be caused due to local field distortions. The main magnetic field (B_0) consists of a strong, highly uniform, static magnetic field running axially along the MRI system with a further static gradient field superimposed. Nuclear Magnetic Resonance (NMR) is stimulated in a specific slice along the field by a radio frequency (RF) pulse according to the Larmor Equation for NMR (Equation 1):

$$\omega_0 = \gamma B_0 \qquad \text{- Equation 1}$$

where ω_0 is the Larmor frequency (resonant frequency), γ is the gyromagnetic ratio (a specific constant for each type of nucleus), and B_0 is the strength of magnetic field (T) experienced by the nucleus. Local fluctuations in the magnetic field due to susceptibility differences between the implant and surrounding tissue alter the local B_0 and distort this selection process thereby warping the resulting image. Figure 1 (a) illustrates how a plane of uniform field strength (purple line) is distorted around a paramagnetic

4

sample. Figure 1 (b) shows how this signal is interpreted as a straight line, resulting in skewing of the MRI image along the B_0 field axis

The second mechanism is dephasing during gradient-echo generation and is unique to this imaging mode. In traditional spin-echo sequences, nuclei gradually de-phase following initial Radio Frequency (RF) excitation due to local magnetic field differences. The echo, required for signal detection, is generated following a 180° RF pulse that effectively reverses this process and causes the nuclei to re-phase (or 'focus') in a manner mirroring de-phasing. In short, if the field variations remain constant, their effect is cancelled out during spin-echo sequences. For a gradient-echo sequence, de-phasing is achieved by applying a field of a known gradient and similarly re-phasing is achieved by reversing this gradient. Local field inhomogeneities are therefore not mitigated in this scenario and can greatly distort the output produced in gradient-echo sequences causing loss of useable signal. Figure 1 (a) indicates the regions of high local field inhomogeneity surrounding a paramagnetic material (orange, dashed regions) and the corresponding loss of signal observed in Figure 1 (b).

Finally, although not specifically relating to susceptibility, the influence of the dynamic (RF) fields used in MRI can induce currents in electrically conductive materials and accentuate these mechanisms. This effect is particularly prominent in conductive loops as described by Faraday's Law of Induction where induced currents produce their own magnetic fields, which in turn distort the surrounding static fields and may further cause or worsen image artefacts.
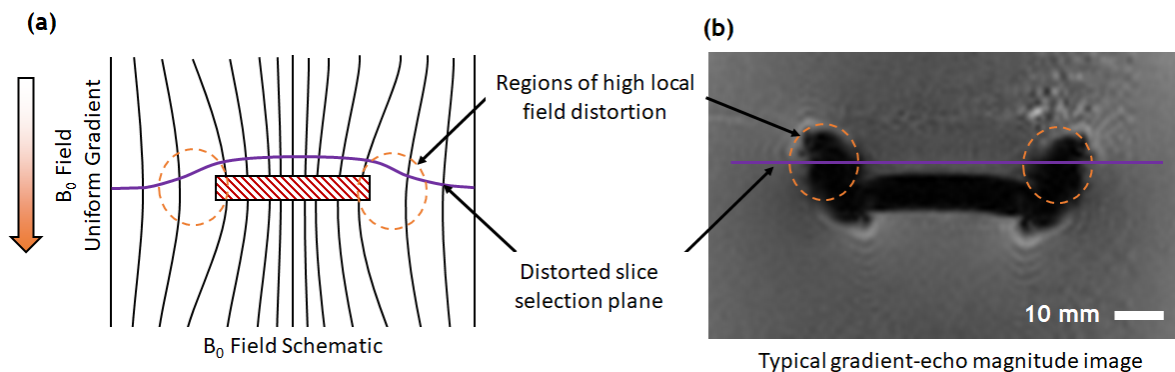

Figure 1: (a) schematic diagram showing the B_0 field distortion surrounding the specimen with regions of high local field distortion and a representation of a distorted slice selection plane indicated. (b) Shows a corresponding MRI slice with the regions of complete signal loss indicated and line representing how the distorted plane is reproduced as a flat plane in the final image.

Several studies, both *in-vitro* and *in-vivo*, have shown susceptibility artefacts become more severe with increasing field strength. Olsrud *et al.* [12] focussed on the appearance of aneurism clip and shunt valve artefacts in a water phantom, which all showed larger volume with field strength increases from 1.5 to 3T. Similarly, Graf *et al.*[13] examined the behaviour of various surgical devices, including a biopsy needle, in a NaCl solution. A study by Radzi *et al.* [14] characterised artefact size surrounding steel and titanium fixation screws, which showed that although the titanium hardware presented significantly smaller artefacts, the change from 1.5 to 3T field strength increased artefact size by approximately 25%. A variety of efforts have been made to quantify the size and severity of artefacts, including a discrete scoring system [15], use of grids or reference geometries [16-18], and simple measurement of length, area, or volume [12, 14, 19-21], however no definitive method has been established and efforts tend to be selected based on what is most appropriate and relevant for the specific study.

There is also a body of research that examines methods to manage and mitigate susceptibility artefacts. A post-processing technique termed 'rectification' presented by Chang and Fitzpatrick [22] combines data from two spin-echo sequences to eliminate image distortion. Despite showing promising results, this method potentially doubles the data acquisition time and is unlikely to be effective in the more sensitive gradient-echo sequences where local field inhomogeneity results in a complete loss of usable signal.

Other investigators have employed non-standard data acquisition techniques to reduce the appearance of susceptibility artefacts. Ramos-Cabrer *et al.* [23] produced promising results using single-point imaging to effectively gather data around a hip prosthesis. Unfortunately, this technique is limited due to the high magnetic gradients and rapid RF pulses, which may cause harmful levels of implant heating if not correctly managed. The use of a pre-polarised MRI scanner by Venook *et al.* [18] showed significant advantages over conventional methods and although these systems are widely available they are currently limited in terms of bore diameter and so are generally unsuitable for full body imaging [11]. Some significant improvements were also made by Viano *et al.* [24] who used a tilted-view angle to reduce the intrusiveness of susceptibility artefacts around both a metal femoral plate and spinal fixation system. A comprehensive review of these techniques is presented by Koch *et al.* [11]. A further

approach is outlined in the modelling work presented by Gao *et al.* [25] who suggested using a diamagnetic material coating to mitigate the magnetic field distortion, thus reducing the MRI artefact. The approach proposed in this study aims to compliment these techniques by fundamentally tailoring the structure of the implant to reduce its magnetic footprint rather than attempting to solve the problem during data acquisition.

Additive Manufacturing (AM) techniques have an inherent design freedom which allows them to produce lightweight and porous structures not possible with traditional manufacturing processes. The current study hypothesises that careful integration of such structures within implants may dramatically reduce the extent and severity of artefacts. Mass reduction as a possible means of MRI artefact reduction can be inferred from work by Shellock [26] showing that a titanium cranial mesh produces only mild artefacts in a 1.5T MRI system and again by Shellock and Valencerina [27] as they demonstrate a lower severity artefact in a septal repair implant with reduced metallic mass. A study presented Levi *et al.* [28] showed significant MRI artefact volume reduction of a porous tantalum cervical spine implant compared to a solid titanium implant of similar geometry and magnetic susceptibility. This research highlights the potential of mass reduction to limit MRI artefact formation and notes that, in this specific application, traditional implants can "produce significant artefact that prevents visualization of the surrounding bone and spinal canal". Levi's study is limited however to a uniform porosity of 80% throughout the component and formed by chemical vapour deposition on to a carbon substrate of the same overall geometry. By comparison AM techniques have the potential to apply lightweight structures in specific regions of a single device and vary the porosity as necessary to ensure that primary functionality is maintained whilst adding a desirable secondary characteristic.

Selective laser melting (SLM) is a widely used metal AM technique in which a computer-controlled laser melts successive layers of metal powder to build up a three-dimensional geometry directly from Computer Aided Design (CAD) file. This process can produce fully dense, functional, and geometrically complex components from Ti-6Al-4V including integration of complex metal lattices (with struts ~ 100 to 400 µm diameter) into components. Lattices produced via this method have attracted significant attention for their structural properties, lightweight capability, and engineered

porosity. The mechanical properties of these lattice structures, including the influence of their relative density and unit cell, have been characterised extensively for biomedical applications [29-32]. Specifically for orthopaedic implants, metal lattices can be tailored to provide effective elastic moduli matching bone to reduce stress-shielding and associated bone loss [33-35]. These porous structures have also been shown to have enhanced osseointegration properties for bone ingrowth and anchoring of the implant [36-39]. A comprehensive review of the current state of AM for biomedical application from both a research and clinical perspective is presented elsewhere by Lowther *et al.*[40].

In summary, this study aims to establish the effectiveness in using AM lightweight Ti-6Al-4V structures to reduce susceptibility artefacts in gradient-echo MRI images. It serves as a proof-of-concept to include such structures intelligently in metal implants where they might best improve the effectiveness of post-operative MRI and thus facilitating early diagnosis of any arising complications.

2. Materials and Methods

2.1. Specimen Design

A fundamental study was designed to systematically investigate the influence on unit cell geometry, size, and overall density of lightweight structures on the severity of susceptibility artefacts in MRI.

Three different lightweight structures were selected along with a single solid specimen of the same overall dimensions to show the behaviour of a fully dense sample. Diamond and octahedral unit cell lattices are commonly used for biomedical applications and can be manufactured by AM without the need for additional supporting structures. A honeycomb design was also selected as it provides a high strength-to-weight ratio in a specific loading direction and is known for being a robust engineering structure. Geometric data was prepared by constructing each unit cell using the Solidworks [41] CAD package and generating a three-dimensional array of copies that were merged in to a single part.

Each geometry was produced with three different unit cell sizes (1, 1.5, and 2 mm for lattices; 2, 4, and 6 mm for honeycomb) and each with three different design element sizes (250, 350, and 450 µm strut diameters for lattices; 0.5, 1, and 1.5 mm wall thicknesses for honeycombs) to provide a range of overall material densities.

All samples measured 42 x 42 x 6 mm in overall dimensions. A summary of the specimens is provided in Table 1 along with diagrammatic representations of the unit cells.
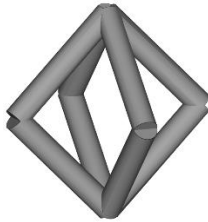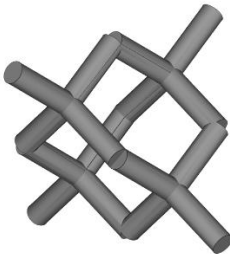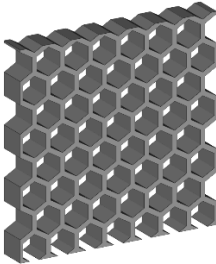
2.2. Specimen Manufacture

Samples were manufactured using a RenAM500M selective laser melting system (Renishaw, UK) located in the Centre for Custom Medical Devices. Samples were produced using spherical Ti-6Al-4V (Grade 23 (RM1) Renishaw, UK) powder provided in the size range of 15 to 53 µm. Layers were processed at a slice thickness of 30 µm using a contour only laser scan strategy for diamond and octahedral lattice designs, and a hatch and contour strategy for honeycomb samples. The laser power and effective scanning speed used for contour scanning was 100W and 1125 mm/s, while 200W and 1100 mm/s were used for hatched regimes, respectively.

Following manufacture specimens were removed from the build substrate by wire electro-discharge machining and hand ground using silicon carbide paper to remove remnants of the underlying supports and ensure an overall dimensional consistency between the test pieces. The mass of each specimen was recorded using a balance (Ohaus AX223, 0.001 g accuracy) and the overall dimensions measured using digital callipers (0.01 mm accuracy). The relative density was calculated compared to that of fully dense Ti-6Al-4V with density, 4.43 g/cm^3 (Table 1).

Table 1: Summary of specimens produced and relative densities
*Note: Solid sample showed lower than expected density due to sample distortion at the corners caused by residual stress from laser processing.

Structure	Unit Cell Size (mm)	Design Strut Dia. (µm) / Wall thickness (mm)	Relative Density (%)
Octahedral	1	250	13.0
		350	40.8
		450	55.3
	1.5	250	5.7
		350	20.5
		450	30.8
	2	250	3.1
		350	12.7
		450	17.6
Diamond	1	250	17.0
		350	48.5
		450	72.1
	1.5	250	7.7
		350	30.5
		450	37.7
	2	250	4.2
		350	18.0
		450	24.5
Honeycomb	2	0.5	37.9
		1	72.1
		1.5	89.1
	4	0.5	20.3
		1	41.4
		1.5	59.2

		0.5	13.6
	6	1	29.4
		1.5	42.4
Solid	N/A	N/A	96.7*

2.3. MRI Measurements

Custom 3D printed polymer lattices (Stratasys, Objet) were prepared as stands for the titanium samples and to provide geometric reference in the collected data. The metal lattices (Figure 2 (a)) were positioned upright in the polymer reference lattice to a depth of approximately 6 mm (Figure 2(b)).

For ease of filling and to facilitate sample changeover, tap water was selected as the phantom media to provide the MRI signal. The water was pre-boiled and allowed to cool to room temperature to remove gas from solution and reduce the formation of air-bubbles within the lattice. Two of the polymer lattice assemblies were attached to the base of each vessel, which were then filled with water so that the metal lattice was fully submerged several centimetres below the surface. The vessel was then placed on a vibrating plate for several minutes until no further air bubbles emerged from the metal lattice.

All MRI data was collected using the 3T Siemens Prisma system (Erlangen, Germany). Each pre-prepared vessel was placed within the system and a scout sequence run to ensure correct positioning and field of view. A 3D gradient-echo imaging sequence with an echo time (T_E) of 1.5 ms provided both magnitude and phase data from 52 contiguous coronal slices with 2 mm thickness with in-plane pixel size of 0.86 x 0.86 mm. A further spin-echo sequence was run with T_E of 5.9 ms, coronal slices at 3.0 mm slice thickness and with in-plane pixel size of 0.98 x 0.98 mm for comparison. Acquisition times were 300 s and 150 s, respectively.
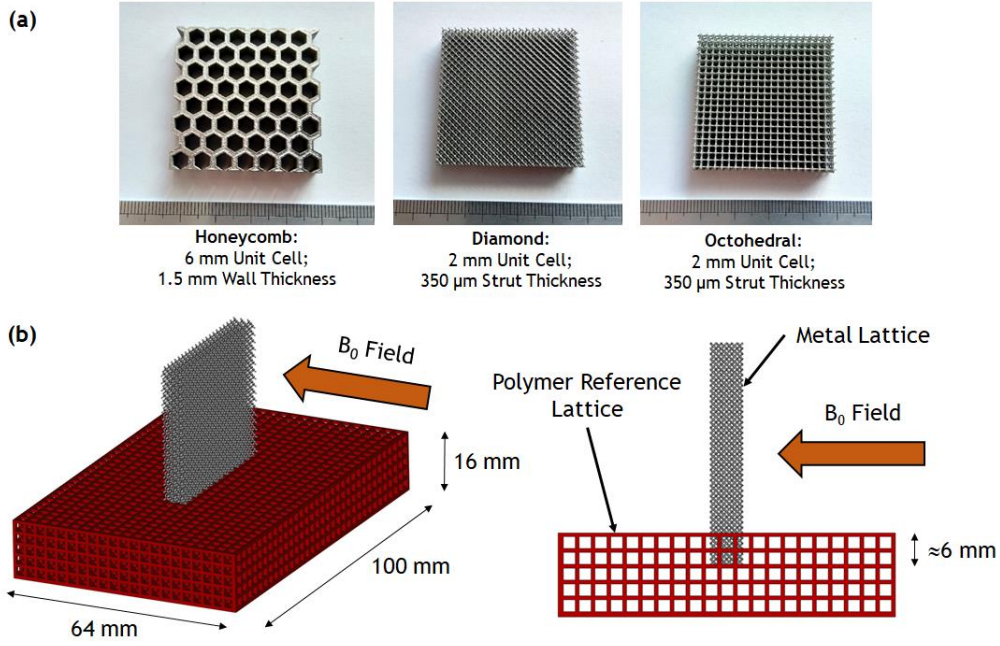
Figure 2: (a) Photographs showing examples of each type of metal lattice; (b) schematic diagram showing the positioning of the metal lattice within the polymer reference lattice and orientation relative to the B_0 filed of the MRI system.

2.4. Image Analysis

All image analysis was carried out using Fiji image analysis software [42]. A uniform threshold was applied to all image stacks when determining artefact volume from the gradient-echo magnitude data. The artefact volume was calculated by subtracting the overall bounding volume of the sample from the threshold volume obtained by image analysis to give just the volume of artefact outside of the boundary of the sample. All pixel value profiles were taken from the coronal slice closest to the midpoint of the specimen.

In order to quantify the image distortion due to B_0 inhomogeneities, the edges of the reference artefact were marked on a visible slice (Red dashed lines, Figure 3(a)). The mid-section slice of the specimen was then selected and the pixel-value profile measured between the midpoints of the two reference lines (denoted by the green line AB in Figure 3(b)). This data was translated so that 0 represented the background value; a plotted version of this pixel value profile is shown in Figure 3(c). A nominal threshold level (-10,000) was then selected outside the range of background noise and the distance between intercepts measured to obtain the region of complete signal loss due to the artefact. The

difference between the midpoint of this region and the expected midpoint of the specimen based on the reference geometry provides a measure of artefact displacement as shown in Figure 3(c).

The extent of the artefacts observed in the phase images was quantified by measuring the distance between the outermost phase wrap for each sample.
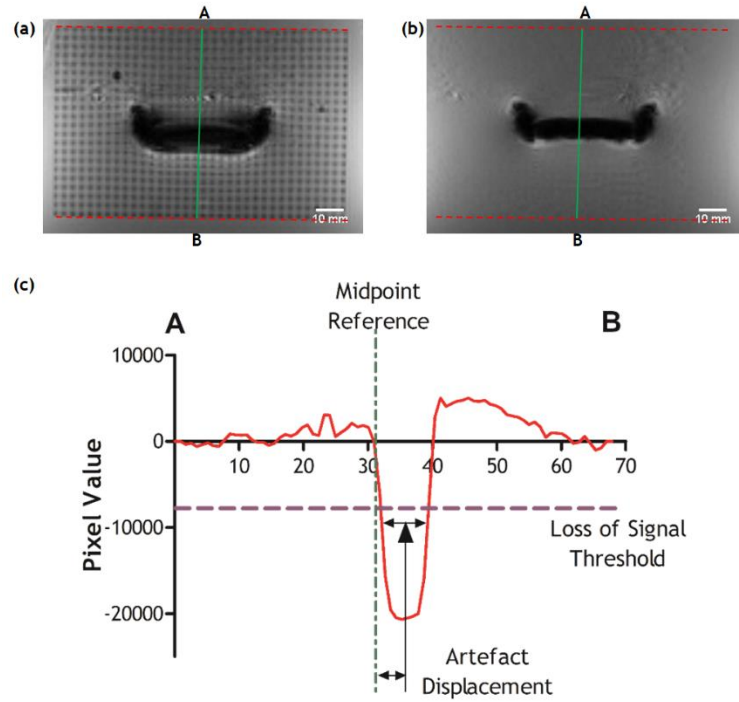

Figure 3: Images showing the method for determining the artefact displacement: (a) edges of reference geometry marked, (b) pixel value profile AB measured at midpoint of specimen, (c) plot showing profile and comparison against expect artefact position.

2.5. Statistical Methods

Where regression analysis was used, the curve fit and R^2 values are provided in the figure caption. Given that only a single MRI data set was produced for each image sequence, error-bars have been plotted based on an estimate of variability due to the image resolution. Where lengths have been presented error-bars show $\pm$ 0.5 pixel which is a reasonable assumption given that distances between pixels were estimated based on linear-interpolation. For volume measurements consistent threshold values have been used between specimens and error bars represent a range of $\pm$ 1 voxel across the entire surface area of the volume to account for noise.

3. Results

Figure 4 shows typical coronal images for diamond lattice structures taken from the gradient-echo sequence for (a) magnitude and (b) phase data, a corresponding (c) spin-echo image, and a (d) gradient-echo longitudinal image showing the vertical section of the specimen. Dark regions in the gradient-echo magnitude data at the edges of the specimens show where the signal has been entirely lost due to the susceptibility artefact and can be seen to increase in area with increasing relative lattice density from 17% to 72%. Figure 4 (c) shows comparative images using the spin echo sequence. This acquisition method does not result in the same regions of complete signal loss as in gradient echo sequences, however both methods show skewing due to field distortion. Figure 4 (a) and (c) serves to highlight the difference between these imaging methods.

Phase images show the extent of disruption caused to the phase of the measured signal. The banding in these images is due to the 'phase-wrapping' effect; phase is the orientation of a vector measured from $-\pi$ to π. The pixel value jumps from its minimum (black) to its maximum (white), or vice versa, each time the received signal passes one of these limits. As with the magnitude data, these images (Figure 4 (b)) show an increased region of influence as the relative density of the samples increases from 17% through 49%, to 72%.

Finally, the longitudinal gradient-echo images Figure 4 (d) show similar 'edge-plumes' of artefact above and below the specimen similar to those seen in the coronal plane.

| | (a) Gradient Echo: Magnitude | (b) Gradient Echo: Phase | (c) Spin Echo: Magnitude | (d) Gradient Echo: Magnitude (Longitudinal) |

17% Density (Diamond; 1 mm Unit; 250 μm Strut Dia.)

49% Density (Diamond; 1 mm Unit; 350 μm Strut Dia.)

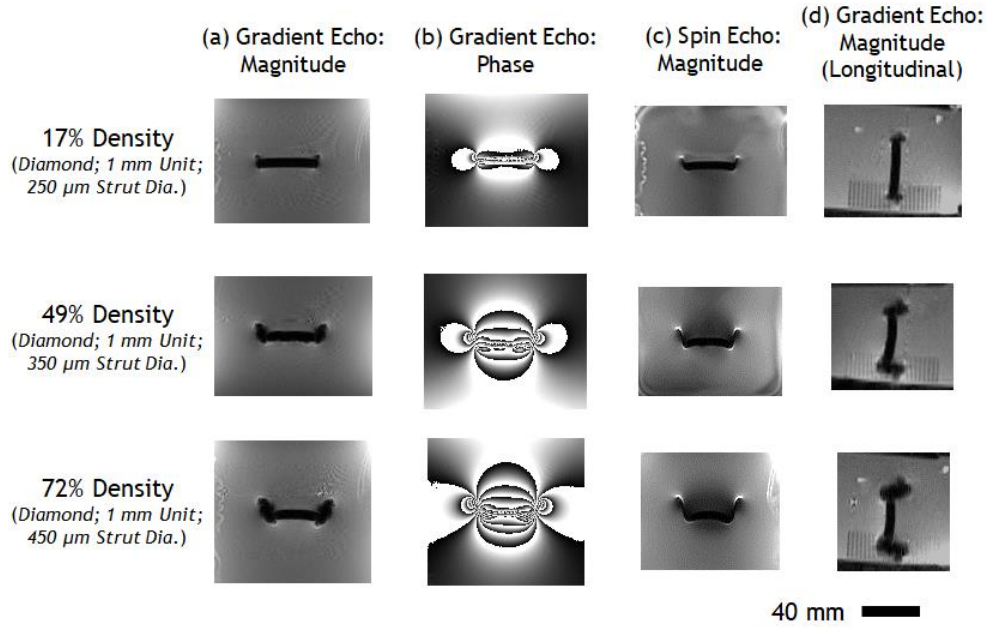72% Density (Diamond; 1 mm Unit; 450 μm Strut Dia.)

40 mm

Figure 4: Typical (a) coronal gradient-echo magnitude, (b) phase, (c) spin-echo magnitude, and (d) longitudinal gradient-echo magnitude images collected by MRI of the metal lattices. Each image type is shown for three lattices of increasing relative density and is representative of the larger dataset in appearance.

Likewise, Figure 5 shows images produced using the gradient-echo sequence for samples of similar relative densities (29.4% - 30.8%) for the three different unit cell designs (octahedral, diamond, and honeycomb). These examples are typical of the dataset as a whole, with metal lattices showing no notable difference in artefact character for magnitude (Figure 5 (a) and (c)) or phase (Figure 5 (b)) images between the two designs (octahedral or diamond). Honeycomb samples showed 'protrusions' of the artefact volume visible in gradient echo magnitude data (see detail of honeycomb sample, Figure 5 (a)) along the edge of the specimen. These features correspond to the honeycomb channels and are more pronounced in the larger cell sizes (6 mm and 4 mm). As a consequence, honeycomb artefacts appear to be more significant than their lattice counterparts for similar sample density.
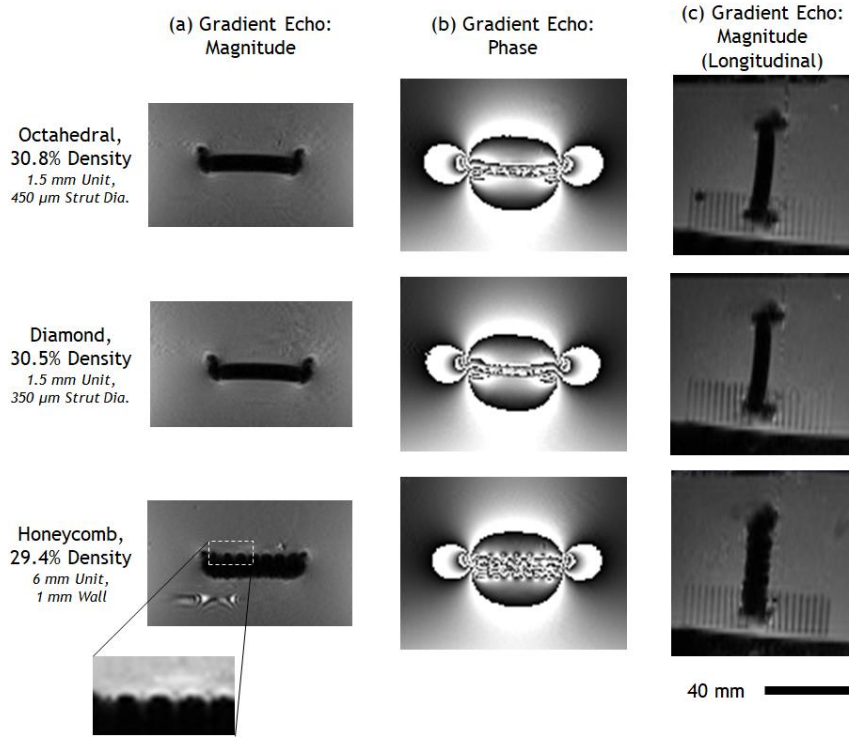
Figure 5: Typical (a) coronal gradient-echo magnitude, (b) phase, and (c) longitudinal gradient-echo magnitude images collected by MRI of the metal samples. Images are shown for samples of similar relative density (29.4% - 30.8%) of the three different unit cell types (Octahedral, Diamond, and Honeycomb).

The volume of the loss of signal region in the gradient-echo magnitude data has been plotted in Figure 6(a) against sample relative density. A linear trendline was fitted to the data with an R^2=0.97, however it was clear that the honeycomb samples lay outside this trend particularly at densities below 60% (green squares Figure 6(a)). Thereby, the trendline was recalculated excluding the honeycomb specimens, which demonstrated an improved correlation, $R^2 = 0.99$. Artefact volume of the honeycomb samples is plotted separately in Figure 6 (d) for each unit cell size. The data shows increasing severity of artefact with cell sizes for the same relative density with 4 mm cells showing an average artefact volume increase of 3700 mm^3 and 6 mm cells an increase of 4300 mm^3 compared to the baseline lattice trend. The typical MRI gradient echo sequence magnitude images for all specimens examined are shown in Supplemental Figure S1.

Analysis of artefact displacement from its expected position revealed a similar positive trend with density (Figure 6(b)). However, a 2nd order polynomial relationship was found to best fit the data with $R^2 = 0.92$ and no obvious outliers were noted. Figure 6(c) shows the distance between the outermost phase wrap as an estimate of the extent of the artefact. A change in gradient was found to coincide with

17

a change in the observed shape of the outer phase-wrap boundary from a flattened to a more rounded shape (see inset images Figure 6 (c)). This transition point occurred at approximately 45% relative density and corresponds to a distance approximately equal to the width of the specimen (42 mm).
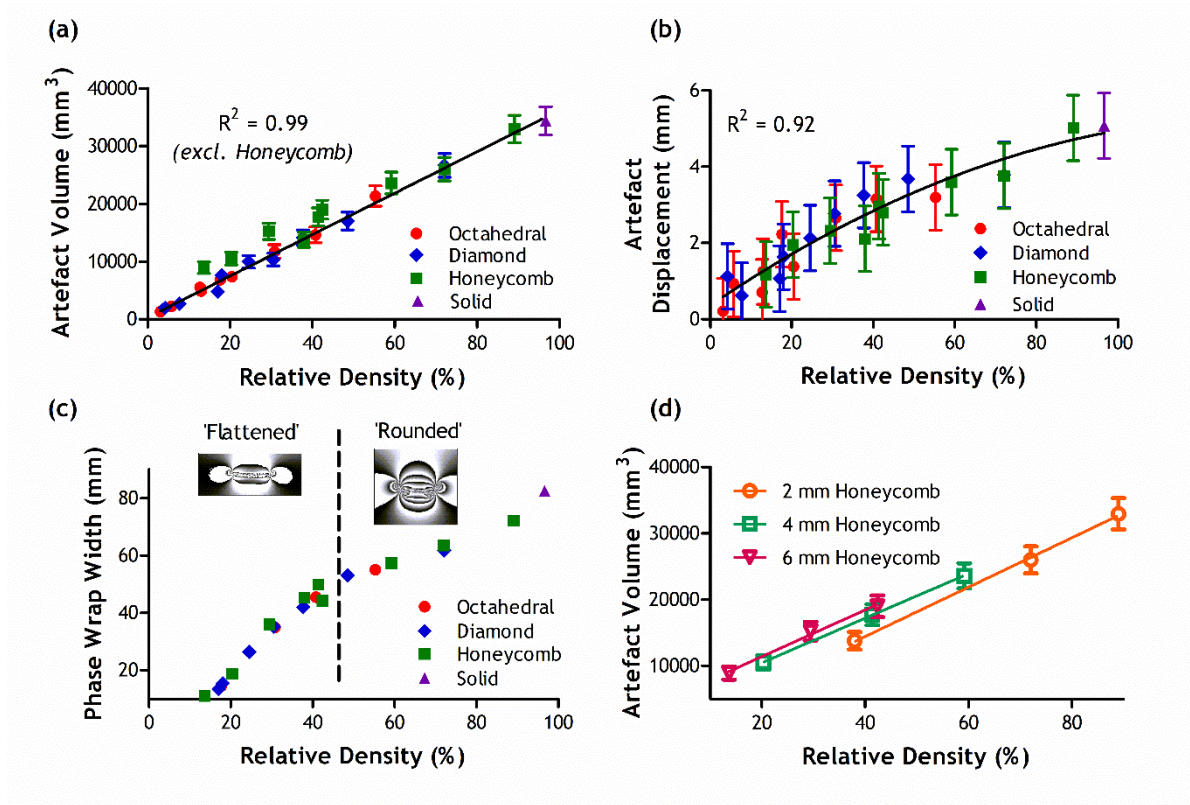

Figure 6: Graphs showing (a) artefact volume for all specimens against relative density. Linear trendline (y = 358.9x) was calculated using the lattice and solid specimens only, $R^2 = 0.99$. (b) Artefact displacement against relative density. 2nd order polynomial trendline (y = 0.3618 + 0.07264x – 0.0002675x^2) was calculated using all data points, $R^2 = 0.92$. (c) Distance between outermost phasewrap in gradient-echo phase data. A shift in artefact character from 'flattened' to 'rounded' is indicated corresponding with a change in gradient at approximately the specimen width. (d) Artefact volume for honeycomb samples against relative density presented for the three different cell sizes.

Finally, MRI data was collected for two representative sections of a cranioplasty plate produced by SLM in Ti-6Al-4V (Figure 7). CAD geometry was cut from a traditional design (green section, Figure 7 (a)) and produced in both solid material (traditional) and with a 55% mass reduction achieved through an applied honeycomb. Both sections were scanned in a similar manner to the cuboidal samples. Analysis showed an approximate 10% reduction in artefact volume of the honeycomb section compared to the traditional; a more accurate measurement was not possible due to the large sample size relative to the water vessel. Figure 7 (b) shows a typical gradient echo magnitude image; significant artefact protrusions surrounding the suture points are clearly visible and labelled.
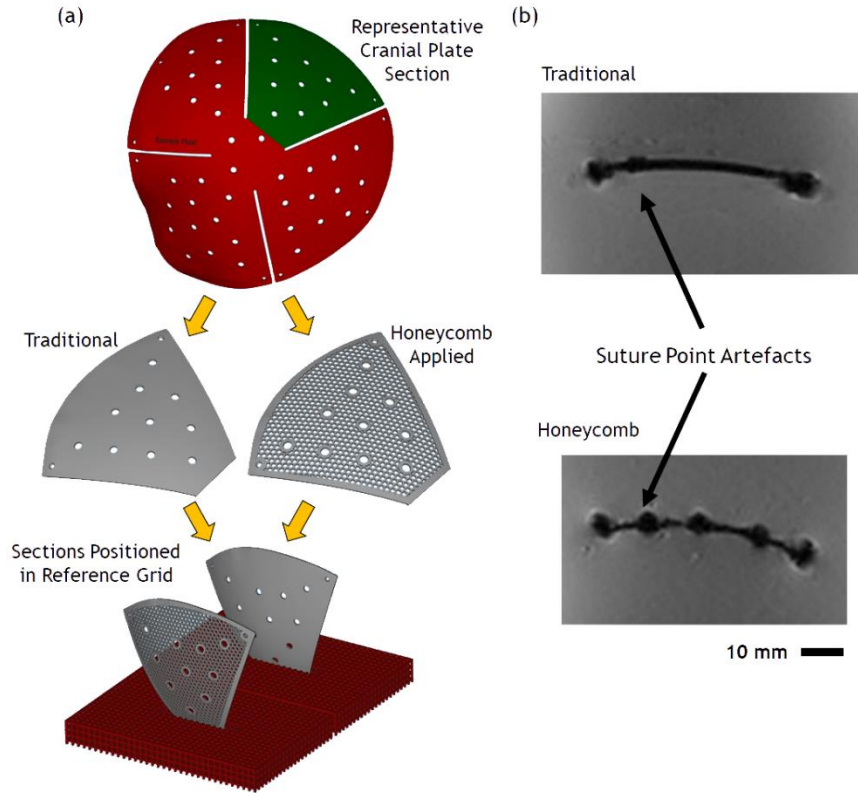
Figure 7: Proof-of-concept showing (a) representative section (green) taken from a traditional cranioplasty plate design and produced by AM in both a 'traditional' and porous honeycomb design. (b) Representative gradient echo magnitude image showing the (top) traditional and (bottom) honeycomb.

4. Discussion

From simple observation of the MR images, it is apparent that increasing the density of the lattice increases the severity of the artefact. Figure 4 (a) shows regions in which no returning signal is detected around the edge of the specimen which increase with increasing density. These appear in both the coronal and longitudinal images suggesting that this effect occurs across the entire sample surface. The overall region of influence is more obvious when observing the phase images (Figure 4 (b)), due to the stark wrapping effect, and shows affected regions extending out perpendicular to the face of the specimen as the relative density increases . Whilst not the focus of this study, it is interesting to note that regions of total signal loss are not observed in the spin-echo sequences (Figure 4 (c)). This can be explained by differences in echo generation between the two modes; the signal from a spin-echo is refocussed with a 180° RF pulse to recover signal loss from local inhomogeneities whereas gradient echo sequences lack this RF refocusing pulse. The spin-echo images Figure 4 (c) show more clearly the

extent of geometric distortion along the B_0 axis due to slice selection errors caused by field inhomogeneity. Fundamentally, these observations can be explained by considering the specimen's interaction with the B_0 field. As shown in Figure 1, loss of signal is present around the sample edges since this is where local field variation is greatest. In turn this field distortion skews the planes of constant field strength along the B_0 axis resulting in slice selection errors and similarly skewed images once the returning signal has been reconstructed.

Figure 6 (a) dramatically shows this relationship of artefact volume against relative density. Setting aside the honeycomb geometries, the linear relationship is remarkably consistent for lattice structures and re-enforces the possibility of utilising these types of structures to strategically reduce MRI artefacts via implant design. In short; a 50% reduction in mass equates to a 50% reduction in artefact severity.

Interestingly, the honeycomb samples were shown to exhibit an increased artefact volume compared with their lattice counterparts at corresponding relative densities (see comparison in Figure 5). Figure 6(d) shows the artefact volume data for the honeycomb samples replotted with best fit lines added for each of the unit cell sizes. It shows a general trend that larger cell sizes in these geometries produce greater artefact volumes than might be expected for their density. The larger than expected artefact volume can be attributed to the protrusions (shown in detail of Figure 5 (a)) that correspond to the unit cell size of the honeycomb sample. Without further investigation it is impossible to confirm the underlying mechanism; however, it is likely to be due to one of two effects. It is possible that the spacing between the walls allow each cell to generate their own distinct field distortion including regions of significant local inhomogeneities that combine to form the observed pattern. Likewise, it may be that each cell of the honeycomb acts as a conductive loop in the exciting RF field. Given the correct relative field orientation, the alternating RF field may induce current to flow around the honeycomb unit cell thus forming a further magnetic field along its axis. The data collected here would potentially support this second hypothesis as Faraday's Law of Induction states:

$$iR = -A \, dB/dt \qquad \text{- Equation 2}$$

where i = induced current, R = resistance of the conductor, A = area enclosed by the conductive loop, dB/dT = rate of change of field strength. Assuming that the RF field is of constant magnitude and frequency then:

$$i \propto A \qquad \text{- Equation 3}$$

This suggests that the larger the honeycomb unit cell, or 'conductive loop', the greater the induced current and internal field strength. The observation the artefact volume increases with unit cell size for honeycomb samples of the same relative density (Figure 6 (d)) supports this explanation but does not confirm it.

The strong positive relationship (2nd order polynomial, R^2 = 0.92) between artefact displacement and relative sample density shown in Figure 6 (b) complements that of the similar positive relationship to artefact volume (Figure 6 (a)). Skewing in the resulting images is driven by error in slice selection caused by field distortions surrounding the paramagnetic material. Despite both the loss of signal and distortion occurring via two different mechanisms, they are both the result of underlying field distortion caused by the paramagnetic material and therefore both show similar trends with respect to relative sample density.

Figure 6 (c) shows the distance between the outermost phase wrap contours with respect to the relative sample density. This graph reiterates the positive trends seen in Figure 6 (a) and (b) albeit not as dramatically as the phase images themselves (Figure 4 (b)). One further feature of interest is the decrease in gradient occurring at approximately 40% relative density. This coincides with a transition in the general shape of the phase wrap from 'flatted' to more 'rounded' (see Figure 6 (c) inset) with the turning point occurring when the width is approximately equal to that of the sample where the wrap profile is approximately semi-circular. Overall geometry therefore has a significant influence on the extent, shape, and location of susceptibility artefacts, an observation that may guide future investigations. Unfortunately, interference between specimens and the edge of the vessel hindered a more in depth analysis of the phase data. Likewise, the poor signal close to the specimen and proximity

21

of successive phase wraps compared to image resolution rendered efforts to 'un-wrap' the data unsuccessful.

Final validation of the technique feasibility showed that on a representative section taken from a traditional cranioplasty design (Figure 7 (a)). A 55% mass reduction provided an approximately 10% reduction in overall artefact volume. The MRI images in Figure 7 (b) presents a generally narrower region of signal loss for the honeycomb design compared to the traditional, however both specimens show large artefact protrusions around the suture holes appearing similar to those previously described for the larger cell size honeycomb samples. The presence of these holes and associated artefact features are likely the reason that the measured artefact reduction is not as significant as a 55% mass reduction might suggest. It should be noted therefore that a lightweight porous cranioplasty, intelligently designed to capitalise on an SLM processing route, would incorporate features to facilitate suture and drainage and as such, this simplistic example could be considered a worst-case scenario. Given the results of this demonstration and the fundamental experiments it is clear that utilising a lattice would yield better results; this design optimisation remains the subject of future investigations.

Utilising AM lightweight porous structures has therefore been shown to provide a promising upstream method to reduce and manage MRI image artefacts surrounding Ti-6Al-4V implants; by reducing the material in the implant, the artefact volume is inherently reduced. Other methods have shown success in the downstream management of artefacts at the acquisition and data processing stages, however each has their own limitations; the rectification method [22] is limited to specific image sequences, single point imaging [23] sequences may result in implant heating, and prepolarised MRI [18] systems are currently limited in bore. By comparison lightweight structures have the potential to reduce artefact severity in any MRI sequence allowing for the most appropriate to be selected based on clinical need. Additionally it may be possible to combine this method with other methods, for example tilted-view angle [24] or diamagnetic coatings [25], to further manage susceptibility artefacts. Of course all implants must be designed to meet the requirements of their primary function and mechanical properties and therefore the application of porous structures purely to reduce susceptibility artefacts will need to be carefully considered on a case-by-case basis. Given the interest in AM lattices for other implant

requirements such as modulus matching [33-35] or osseointegration [36-39], it is likely that many implants may be able to benefit in the future either as a primary or secondary effect of using AM lattices in designs.

5. Conclusions

Ti-6Al-4V lightweight structures produced by selective laser melting have been shown to reduce the severity of MRI susceptibility artefacts compared to solid material. For octahedral and diamond lattice structures artefact volume varies linearly with relative density ($R^2 = 0.99$), broadly a 50% reduction in mass showed 50% reduction in artefact volume. In contrast, honeycomb structures display a marginally higher than expected artefact volume for their relative density when examining the larger (6 mm, 4300 mm^3 increase; 4 mm, 3700 mm^3 increase) unit cell sizes. Interestingly, artefact displacement also displayed a strong correlation with sample density ($R^2 = 0.92$), due to distortion of the B_0 field caused by the metal lattice resulting in slice selection skewing.

Phase images highlight the extent of field disruption caused by the metal samples, and measurements of their severity supported the same positive correlation with relative density as seen in the magnitude data. The overall shape of the phase disruption appeared to be governed by both the density and geometry of the sample which will prove an interesting area of study in future investigations.

Crucially, the unified parameter, relative density, rather than unit cell type, unit cell size, or strut diameter has been shown to drive the artefact behaviour surrounding the lattice specimens.

Overall this experimental campaign has shown that AM lightweight structures may be an effective upstream method of reducing susceptibility artefacts in Ti-6Al4V implants. A representative cranioplasty demonstrator with a honeycomb structure was shown to reduce artefact volume by 10%. It is acknowledged however, that application of lightweight structures would need to be carefully considered to ensure the implant is still able to meet its primary functionality.

By exploiting the design freedoms of additive manufacturing to intelligently integrate complex lightweight geometries in implants, the subsequent imaging of underlying anatomical structures, and crucially diagnostic accuracy, may be greatly improved.

6. Acknowledgements

7. References

[1] A. Patel, G. Pavlou, R.E. Mújica-Mota, A.D. Toms, The epidemiology of revision total knee and hip arthroplasty in England and Wales: A comparative analysis with projections for the United States. a study using the national joint registry dataset, Bone and Joint Journal 97-B(8) (2015) 1076-1081.

[2] PRNewswireUS, Worldwide Metal Implants & Medical Alloys Market 2019-2024: Analysis on Industry Size & Future Growth Potential for Various Segments - ResearchAndMarkets.com, 2019.

[3] J.H. Duyn, The future of ultra-high field MRI and fMRI for study of the human brain, NeuroImage 62(2) (2012) 1241-1248.

[4] B.M. Dale, M.A. Brown, R.C. Semelka, MRI : Basic Principles and Applications, John Wiley & Sons, Incorporated, New York, UNITED KINGDOM, 2015.

[5] A.G. Sinclair, D.J. Scoffings, Imaging of the Post-operative Cranium, RadioGraphics 30(2) (2010) 461-482.

[6] T. Tamaki, T. Eguchi, M. Sakamoto, A. Teramoto, Use of diffusion-weighted magnetic resonance imaging in empyema after cranioplasty, British Journal of Neurosurgery 18(1) (2009) 40-44.

[7] F. Girgis, B. Walcott, C.-S. Kwon, S. Sheth, W. Asaad, B. Nahed, E. Eskandar, J.-V. Coumans, The Absence of Fever or Leukocytosis Does Not Exclude Infection Following Cranioplasty, Canadian Journal of Neurological Sciences 42(4) (2015) 255-259.

[8] S.M. Greenberg, M.W. Vernooij, C. Cordonnier, A. Viswanathan, R. Al-Shahi Salman, S. Warach, L.J. Launer, M.A. Van Buchem, M.M. Breteler, G. Microbleed Study, Cerebral microbleeds: a guide to detection and interpretation, Lancet Neurol 8(2) (2009) 165-174.

[9] L. Lee, J. Ker, B.L. Quah, N. Chou, D. Choy, T.T. Yeo, A retrospective analysis and review of an institution's experience with the complications of cranioplasty, British Journal of Neurosurgery 27(5) (2013) 629-635.

[10] P. Frassanito, F. Fraschetti, F. Bianchi, F. Giovannenze, M. Caldarelli, G. Scoppettuolo, Management and prevention of cranioplasty infections, Child's nervous system : ChNS : official journal of the International Society for Pediatric Neurosurgery (2019).

[11] K.M. Koch, B.A. Hargreaves, K.B. Pauly, W. Chen, G.E. Gold, K.F. King, Magnetic resonance imaging near metal implants, Hoboken, 2010, pp. 773-787.

[12] J. Olsrud, J. Lätt, S. Brockstedt, B. Romner, I.M. Björkman-Burtscher, Magnetic resonance imaging artifacts caused by aneurysm clips and shunt valves: Dependence on field strength (1.5 and 3 T) and imaging parameters, Journal of Magnetic Resonance Imaging 22(3) (2005) 433-437.

[13] H. Graf, U.A. Lauer, A. Berger, F. Schick, RF artifacts caused by metallic implants or instruments which get more prominent at 3 T: an in vitro study, Magnetic Resonance Imaging 23(3) (2005) 493-9.

[14] S. Radzi, G. Cowin, M. Robinson, J. Pratap, A. Volp, M.A. Schuetz, B. Schmutz, Metal artifacts from titanium and steel screws in CT, 1.5T and 3T MR images of the tibial Pilon: a quantitative assessment in 3D, Quantitative Imaging in Medicine and Surgery 4(3) (2014) 163-172.

[15] T. Ernstberger, G. Heidrich, H.-M. Klinger, M.H. Baums, Score based assessment of implant-related post fusion MRI artifacts focused on different interbody disc spacers: An in vitro study, Open Journal of Clinical Diagnostics Vol.02No.02 (2012) 7.

[16] M.F. Koff, P. Shah, K.M. Koch, H.G. Potter, Quantifying image distortion of orthopedic materials in magnetic resonance imaging, Journal of Magnetic Resonance Imaging 38(3) (2013) 610-618.

[17] K.M. Koch, J.E. Lorbiecki, R.S. Hinks, K.F. King, A multispectral three-dimensional acquisition technique for imaging near metal implants, Magnetic Resonance in Medicine 61(2) (2009) 381-390.

[18] R.D. Venook, N.I. Matter, M. Ramachandran, S.E. Ungersma, G.E. Gold, N.J. Giori, A. Macovski, G.C. Scott, S.M. Conolly, Prepolarized magnetic resonance imaging around metal orthopedic implants, Magnetic Resonance in Medicine 56(1) (2006) 177-186.

[19] A. Illanes, J.W. Krug, M. Friebe, Assessing MRI susceptibility artefact through an indicator of image distortion, Current Directions in Biomedical Engineering 2(1) 427-431.

[20] F. Khursheed, F. Rohlffs, S. Suzuki, D. Kim, T. Ellmore, Artifact quantification and tractography from 3T MRI after placement of aneurysm clips in subarachnoid hemorrhage patients, BMC Medical Imaging 11(1) 19.

[21] U. Wonneberger, B. Schnackenburg, F. Streitparth, T. Walter, J. Rump, U. Teichgräber, Evaluation of Magnetic Resonance Imaging-Compatible Needles and Interactive Sequences for Musculoskeletal Interventions Using an Open High-Field Magnetic Resonance Imaging Scanner, CardioVascular and Interventional Radiology 33(2) (2010) 346-351.

[22] H. Chang, J.M. Fitzpatrick, A technique for accurate magnetic resonance imaging in the presence of field inhomogeneities, Medical Imaging, IEEE Transactions on 11(3) (1992) 319-329.

[23] P. Ramos-Cabrer, J.P.M. van Duynhoven, A. Van der Toorn, K. Nicolay, MRI of hip prostheses using single-point methods: In vitro studies towards the artifact-free imaging of individuals with metal implants, Magnetic Resonance Imaging 22(8) (2004) 1097-1103.

[24] A.M. Viano, S.A. Gronemeyer, M. Haliloglu, F.A. Hoffer, Improved MR imaging for patients with metallic implants☆, Magnetic Resonance Imaging 18(3) (2000) 287-295.

[25] K. Yanhui Gao, A. Muramatsu, K. Kushibe, A. Yamazaki, T. Chiba, T. Yamamoto, Reduction of Artifact of Metallic Implant in Magnetic Resonance Imaging by Coating of Diamagnetic Material, Magnetics, IEEE Transactions on 45(10) 4837-4840.

[26] F.G. Shellock, Metallic neurosurgical implants: Evaluation of magnetic field interactions, heating, and artifacts at 1.5-Tesla, Journal of Magnetic Resonance Imaging 14(3) (2001) 295-299.

[27] F.G. Shellock, S. Valencerina, Septal repair implants: evaluation of magnetic resonance imaging safety at 3 T, Magnetic Resonance Imaging 23(10) (2005) 1021-1025.

[28] D.O.A. Levi, G.W. Choi, J.P. Keller, E.J. Heiserman, K.H.V. Sonntag, A.C. Dickman, The Radiographic and Imaging Characteristics of Porous Tantalum Implants Within the Human Cervical Spine, Spine 23(11) (1998) 1245-1250.

[29] S. Ahmadi, S. Yavari, R. Wauthle, B. Pouran, J. Schrooten, H. Weinans, A. Zadpoor, Additively Manufactured Open-Cell Porous Biomaterials Made from Six Different Space-Filling Unit Cells: The Mechanical and Morphological Properties, Materials 8(4) (2015) 1871.

[30] S.M. Ahmadi, G. Campoli, S. Amin Yavari, B. Sajadi, R. Wauthle, J. Schrooten, H. Weinans, A.A. Zadpoor, Mechanical behavior of regular open-cell porous biomaterials made of diamond lattice unit cells, Journal of the Mechanical Behavior of Biomedical Materials 34 (2014) 106-115.

[31] J. Kadkhodapour, H. Montazerian, A.C. Darabi, A.P. Anaraki, S.M. Ahmadi, A.A. Zadpoor, S. Schmauder, Failure mechanisms of additively manufactured porous biomaterials: Effects of porosity and type of unit cell, Journal of the Mechanical Behavior of Biomedical Materials 50 (2015) 180-191.

[32] A. du Plessis, I. Yadroitsava, I. Yadroitsev, S.G. le Roux, D.C. Blaine, Numerical comparison of lattice unit cell designs for medical implants by additive manufacturing, (2018) 1-16.

[33] O.L.A. Harrysson, O. Cansizoglu, D.J. Marcellin-Little, D.R. Cormier, H.A. West, Direct metal fabrication of titanium implants with tailored materials and mechanical properties using electron beam melting technology, Materials Science & Engineering C 28(3) (2008) 366-373.

[34] S. Arabnejad, B. Johnston, M. Tanzer, D. Pasini, Fully porous 3D printed titanium femoral stem to reduce stress-shielding following total hip arthroplasty, Journal of Orthopaedic Research 35(8) (2017) 1774-1783.

[35] A. Rahimizadeh, Z. Nourmohammadi, S. Arabnejad, M. Tanzer, D. Pasini, Porous architected biomaterial for a tibial-knee implant with minimum bone resorption and bone-implant interface micromotion, Journal of the Mechanical Behavior of Biomedical Materials 78 (2018) 465-479.

[36] S. Van Bael, Y.C. Chai, S. Truscello, M. Moesen, G. Kerckhofs, H. Van Oosterwyck, J.P. Kruth, J. Schrooten, The effect of pore geometry on the in vitro biological behavior of human periosteum-derived cells seeded on selective laser-melted Ti6Al4V bone scaffolds, Acta Biomaterialia 8(7) (2012) 2824-2834.

[37] D.A. Hollander, M. Von Walter, T. Wirtz, R. Sellei, B. Schmidt-Rohlfing, O. Paar, H.-J. Erli, Structural, mechanical and in vitro characterization of individually structured Ti–6Al–4V produced by direct laser forming, Biomaterials 27(7) (2006) 955-963.

[38] T. Douglas, P. Warnke, B. Temel, P. Wollny, S. Becker, I. Springer, J. Wiltfang, S. Sivananthan, Rapid Prototyping: Porous Titanium Alloy Scaffolds Produced by Selective Laser Melting (SLM) for Bone Tissue Engineering, Tissue Eng. Part A 15(5) (2009) O7-O8.

[39] W. Xue, B.V. Krishna, A. Bandyopadhyay, S. Bose, Processing and biocompatibility evaluation of laser processed porous titanium, Acta Biomaterialia 3(6) (2007) 1007-1018.

[40] M. Lowther, S. Louth, A. Davey, A. Hussain, P. Ginestra, L. Carter, N. Eisenstein, L. Grover, S. Cox, Clinical, industrial, and research perspectives on powder bed fusion additively manufactured metal implants, Additive Manufacturing 28 (2019) 565-584.

[41] Solidworks, Dassault Systems, 2013.

[42] J. Schindelin, I. Arganda-Carreras, E. Frise, V. Kaynig, M. Longair, T. Pietzsch, S. Preibisch, C. Rueden, S. Saalfeld, B. Schmid, J.-Y. Tinevez, D.J. White, V. Hartenstein, K. Eliceiri, P. Tomancak, A. Cardona, Fiji: an open-source platform for biological-image analysis, Nature Methods 9 (2012) 676.